Study of carbon-doped Mn$_3$Ga thin films with enhanced magnetization

José T. Holguín-Momaca[a], Rocío M. Gutiérrez Pérez[a], Armando Reyes-Rojas[a], Francisco Espinosa-Magaña[a], Ricardo López Antón[b], and Sion F. Olive-Méndez[a,*]

[a]*Centro de Investigación en Materiales Avanzados, S.C. (CIMAV) Miguel de Cervantes No. 120, C.P. 31136, Chihuahua, Chih., Mexico.*
[b]*Instituto Regional de Investigación Científica Aplicada (IRICA) and Departamento de Física Aplicada, Universidad de Castilla-La Mancha, 13071 Ciudad Real, Spain*

Electronic mail: sion.olive@cimav.edu.mx

Abstract

Carbon-doped Mn$_3$Ga thin films were grown on Si/SiO$_2$ substrates using rf magnetron sputtering technique and they present an enhancement of their magnetization. In this work we focus on the structural stress, theoretical calculations and magnetization analysis (using both Bloch's and Kneller's laws). The residual stress component has been calculated by means of x-ray diffraction in gracing incidence, using the χ method for multiple crystallographic reflections. We have observed an increase of the cell volume or positive (tensile) strain, which is higher near the surface of the film. The existence of induced magnetism in Mn$_3$GaC$_{0.25}$, with C entering in interstitial positions has been investigated by first-principles calculations, using the projector-augmented-wave method, within the generalized gradient approximation. Spin charge distributions and magnetic moments associated with each ion, were analyzed by performing a Bader charge analysis. Noteworthily, in spite of being a thin film, the magnetic behavior of the sample can be well described considering it formed by magnetic nanoparticles. Magnetic field and temperature dependence of the magnetization measurements were used to evaluate the Bloch and Kneller exponents, showing that dipolar interactions take place between Mn$_3$GaC$_{0.25}$ nanoparticles.

Keywords: Thin films and multilayers; Magnetic properties; Point defect; Density functional theory

1 Introduction

One of the major challenges in spintronics is the development of functional materials suiting the requirements of faster operation, lower power consumption and the capacity to store information in a non-volatile manner. Several methods are used to control spin transport and manipulation in magnetic and non-magnetic metals and semiconductors, as, e.g., electric field assisted magnetization [1], creation of spin-polarized currents induced by polarized light [2], room temperature spin injection into semiconductors [3], etc. Spin-transfer torque (STT) is a process to switch the orientation of the magnetization of ferromagnetic (FM) thin films, for example in magnetic tunnel junctions (MTJ), which are the core of magnetic random access memories. A material that has been proposed to elaborate the free layer of MTJs is the tetragonal phase $D0_{22}$ of Mn_3Ga, which is ferrimagnetic (FiM) with a bulk magnetization of 110 kAm^{-1}, a Curie temperature of 770 K, high perpendicular magnetic anisotropy (PMA) of 0.89×10^6 Jm^{-3}, and high coercivity [4]. In particular, low magnetization and high PMA are requirements to reduce the time and the length of a spin polarized pulse to switch the magnetic orientation in the STT process. The crystalline structure of Mn_3Ga has two Mn sublattices: Mn_X and Mn_Y, which correspond to the positions X and Y of a full Heusler alloy X_2YZ, and the Z position is for Ga. The Mn magnetic moments in each X and Y sublattices are $1.6\mu_B$ and $-2.8\mu_B$, respectively. The total magnetic moment per cell, containing 6 Mn atoms and 2 Ga atoms, is $0.8\mu_B$. In a previous work we have grown carbon-doped Mn_3Ga thin films with the aim to enhance the magnetization from its bulk value [5]. Those results indicate that a saturation magnetization (M_s) of 200 kAm^{-1} is reached with a carbon concentration of 0.25 at.% (i.e., a formula corresponding to $Mn_3GaC_{0.25}$). Also, theoretical calculations show that the most stable position for C atoms are the interstitial sites at the octahedrons formed by Mn atoms and one Ga atom. The magnetic field dependence on the magnetization, M-H loops, are anhysteretic at room temperature indicating a decrease of the T_C accompanied by an increase of the M_s. It is important, for a further spintronic application, to understand the mechanism that produces the enhancement of M_s and to describe the structural and magnetic properties of C-doped Mn_3Ga thin films.

In this work we study the effect of carbon doping on Mn_3Ga thin film, especially on its magnetic properties. We focus on the quantification of the strain, the modification of the magnetic moments of the involved atoms, including Ga and C and an analysis of the *M-H* curves, using Bloch's and Kneller's equations.

2 Experimental methods

Thin films were grown in a magnetron sputtering system with a base pressure better than 5×10^{-8} Torr. Targets were eroded by Ar gas using radio frequency power sources at an operation pressure of 3 mTorr. Co-sputtering was achieved from a homemade Mn_3Ga target and a commercial high-purity C target eroded at 25 and 37 W, respectively. The deposition rate including the C flux is 0.5 nm/min. The selected growth rate of C is calibrated in order to obtain the composition $Mn_3GaC_{0.25}$, which leads to a high magnetization of 210 kAm^{-1}, very close to 200 kAm^{-1} reported earlier [5]. Structural Characterization was carried out using x-ray diffraction (XRD) with a PANalytical X'Pert equipment, Cu-Kα radiation, and an Empyrean diffractometer Cu x-ray tube with 1.54056 Å of wavelength with programmable χ, ϕ, and *z* axes to identify the phase of the C-doped Mn_3Ga thin films and to quantify the strain. Density-functional theory calculations were performed using the Vienna Ab Initio Simulation Package (VASP) [6,7]. The electronic structure has been calculated using projector augmented-wave (PAW) method [7,8,9] within the Generalized Gradient Approximation (GGA) exchange-correlation energy in the Perdew-Burke-Ernzerhof (PBE) approach [10]. The starting structure is the tetragonal Mn_3Ga, with space group *I*4/*mmm*. This structure contains two Mn_3Ga formula units. The Ga atom is located at (0,0,0) and the Mn atoms occupy two different positions. The first is located at (½, ½, 0) and the second at (½, 0, ¼). The lattice parameters are $a = b = 3.91$ Å and $c = 7.10$ Å. In order to generate the $Mn_3GaC_{0.25}$, we built a $2 \times 2 \times 2$ supercell with 64 non-equivalent atoms. Next, we introduce 4 C atoms, entering in interstitial sites, in the planes containing only Mn atoms, as can be seen in Fig. 4(b). Once the interstitial sites are generated, the structure was fully relaxed to the equilibrium configuration until the Hellmann-Feynman forces were smaller than 0.001 eV/Å. The summation over the Brillouin zone was limited to a $6 \times 6 \times 6$ k-points mesh, within a Monkhorst Pack scheme, which resulted in 27 k-points in the

irreducible part of the Brillouin zone (IBZ). Convergence criterion was set at 10^{-5} eV for the calculation. Finally, *M-H* loops were measured at 300, 250, 150, 50 and 10 K with a superconducting quantum interference device (SQUID) from Quantum Design in order to calculate the Bloch's and Kneller's exponents.

3 Results and discussion

3.1. Structural and strain analysis

The tetragonal phase $D0_{22}$ of Mn_3Ga was identified by XRD in grazing incidence. No phase changes are observed upon C-doping (from the tetragonal phase of Mn_3Ga to the antiperovskite phase of Mn_3GaC, which usually appears at high C concentrations i.e., $Mn_3GaC_{0.8}$ [11]). The peaks are slightly shifted towards the left, compared to the theoretical values of undoped Mn_3Ga, indicating a lattice expansion of the crystalline structure due to the introduction of C into the voids of the octahedron formed by four Mn atoms in the axial positions, one Mn atom at the upper vertex and a Ga atom at the lower vertex [5]. Scherrer formula has been used to calculate the average size of the crystallites composing the film. The length along the (002) direction is 23.6 nm and along the (200) direction is 20.0 nm, which indicates that the nanoparticles (NPs) composing the film are prolate spheroids.
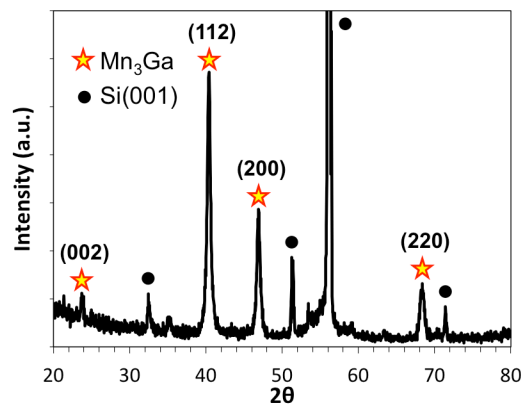

Fig. 1. XRD diffraction pattern of a 50-nm thick $Mn_3GaC_{0.25}$ thin film collected in grazing incidence. The peaks indicate that the tetragonal phase is preserved; neither secondary phases nor antiperovskite phases are observed.

Gracing incidence x-ray diffraction patterns were used to determinate the residual stress component. In order to determinate its variation with the depth (τ), the instrumental ω angle was fixed in 0.5, 1.0 and 1.5 degrees (after the critical angle) to keep a small x-ray penetration in the thin film. The S_1 and ½S_2 x-ray elastic constants were obtained using the isotropic elastic constants E, Young's modulus and υ, Poisson's ratio, which were obtained experimentally from a Nano Indenter G200 (E = 250 MPa; υ = 0.3). These values are smaller than those calculated by other authors using first-principles for a Ni₂MnGa tetragonal symmetry [12] (144 GPa and υ = 0.342) without C [13]. Since the elastic constants are related between them, their determination can be done therefore from equations 1 and 2 [14].

$$S_1 = \frac{-\upsilon}{E} \tag{1}$$

$$\frac{1}{2}S_2 = \frac{1+\upsilon}{E} \tag{2}$$

Here, the χ method from multiples {hkl} crystallographic reflections were employed to determinate the residual stress component from equation 3 [15].

$$\varepsilon_\psi^{hkl} = \left(2S_1^{hkl} + \frac{1}{2}S_2^{hkl}\sin^2\psi\right)\langle\sigma_\parallel^S\rangle \tag{3}$$

where the $\varepsilon_{\phi\psi}^{hkl}$ is measured as a function of the ψ angle, and the stress $\langle\sigma_\parallel^S\rangle$ can be obtained from the slope of a fitted straight line. As can be seen in Fig. 2, the XRD pattern of Mn₃Ga, which was simulated from the results of lattice constant (not thin films) from other authors [16], and using the site symmetry of the Wyckoff positions 2a, 2b and 4d for a crystal structure type as Al₃Ti, shows a perfect tetragonal structure with symmetry I₄/mmm. Hence, this pattern has been considered for our calculations as a strain-free unit cell parameter. Mismatch distributions of (112) and (004) crystallographic reflections are evident, between experimental and calculated XRD pattern. Both reflections show a hkl shift to the left side of the XRD experimental pattern; consequently, there is an increase of volume cell or positive strain ε. This strain is confirmed by the residual stress measurement (see Fig. 3 and

inset), where the $\varepsilon_{\phi\psi}^{hkl}$ versus $Sin^2\psi$ plots for all depths (τ) tested show a linear dependence and positive slopes, which indicate the presence of effective tensile stresses in the Mn₃GaC₀.₂₅ tetragonal lattice. It was found experimentally that as the thin film is deposited, the direction of the residual stress component is in tension, σ_ϕ = 7880 kPa at ω = 0.5 deg. On the other hand, when the depth of x-ray beam, τ, is increased even more, the residuals stress component was 8442 kPa and 8443 kPa for ω = 1 and 1.5, respectively (inset in figure 3 shows the values calculated as the τ is increased).
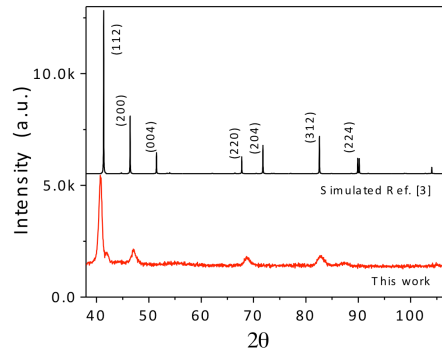
Fig. 2. X-ray diffraction patterns of C-doped Mn₃Ga thin film simulated from the lattice constant [16], and experimental from this work.
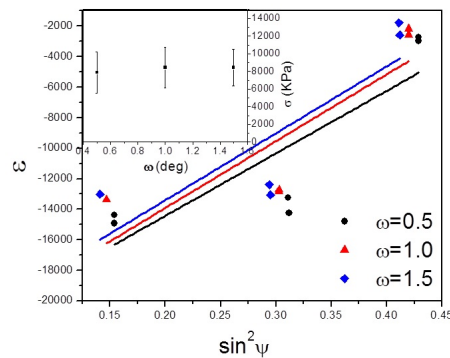

Fig. 3. Residual stress component as a function of the ω angle. The inset shows the variation of the residual stress component as the x-ray beam depth increases.

Therefore, when the x-ray depth increases for values higher or equal than ω = 1, the residual stress at tension remains unchanged, indicating a stress relaxation as the Si(001)

substrate is approaching. Also, the values of residual stress depend of the lattice constant mismatch of the silicon substrate (5.45 Å) and the antiperovskite ($a = b = 3.91$ Å and $c = 7.10$ Å); however, the results indicate that as it is approach to the boundary, it increases its magnitude, therefore the C atoms into the crystal structure act positively decreasing the residual stress and avoiding possible cracks over the thin film surface.

3.2. Computational calculations

The obtained lattice parameters, after relaxation, for the $2 \times 2 \times 2$ supercell, with interstitial C are $a = 7.578$, $b = 7.535$ and $c = 14.428$ Å, showing that the structure changes from tetragonal to orthorhombic, due to C doping (see Fig. 4).
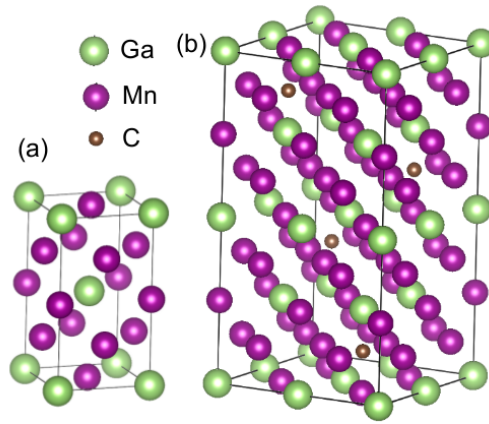

Fig. 4. (a) Crystal structure of tetragonal Mn_3Ga. (b) Crystal structure of $Mn_3GaC_{0.25}$, before the optimization process.

The calculations show a ground state with FM order. From the Bader analysis of charges, a total magnetic moment of $20.96\mu_B$ (221.7 kAm^{-1}) was obtained. This FM order comes mainly from Mn. We have three different kinds of ions, according to the plane they are located. The Mn ions located in the planes containing C atoms, and labeled Mn_I possess a magnetic moment in the range $2.38 - 2.96$ μ_B, whereas Mn ions in planes containing Ga atoms can have a magnetic moment of -4.09 μ_B (Mn_{II}) or -2.72 μ_B (Mn_{III}), the latter for Mn ions located near C atoms.

On the other hand, Ga atoms contribute with -0.29 μ_B or -0.14 μ_B. Finally, C atoms acquire a magnetic moment of -0.29 μ_B. A net magnetic moment arising from 32 Mn_I, 12 Mn_{II}, 4 Mn_{III}, 16 Ga and 4 C atoms gives the previously stated value of 20.96 μ_B/u.c. Fig. 5(a) shows the total density of states of the supercell, as well as the partial density of states for d orbitals of Mn_I, Mn_{II} and Mn_{III}, showing that the main contribution to the magnetic moment comes from Mn ions. For Mn_I, spin-up d-orbitals are forced to move to the valence band, contributing to the majority spin, whereas for Mn_{II} and Mn_{III}, spin-down d-orbitals domain minority spin in valence band. The number of Mn_I ions dominates the final result for a net spin-up magnetic moment. Furthermore, the total density of states shows a metallic-like character of the structure. Fig. 5(b) shows the partial density of states for s and p orbitals of Ga and C atoms. Both orbitals contribute with a small spin-down magnetic moment.
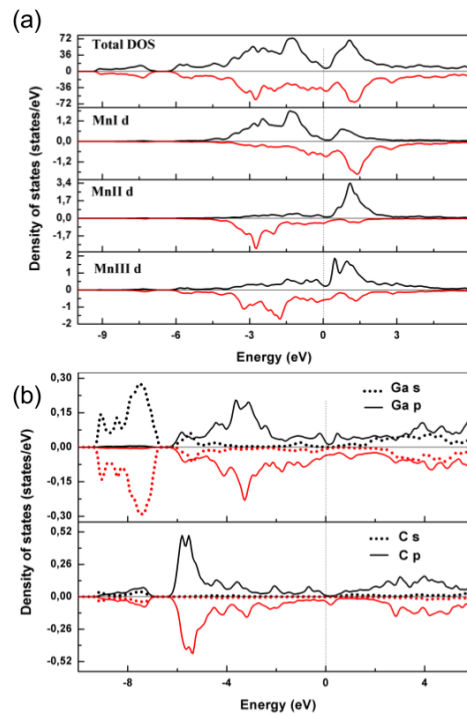

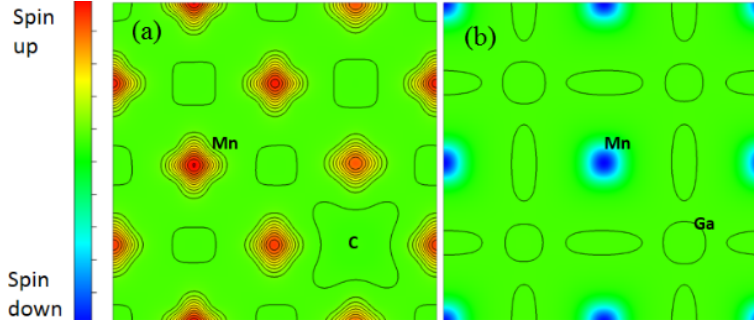Fig. 5. (a) Total density of states of $Mn_3GaC_{0.25}$. (b) Partial density of states for Mn-d orbital.

Fig. 6. Spin density graphs for $Mn_3GaC_{0.25}$ on a plane: (a) containing Mn and C atoms; (b) containing Mn and Ga atoms

3.3. Magnetization analysis

Figures 7(a) and 7(b) show the SQUID *M-H* curves measured at 300, 250, 150, 50 and 10 K, with the applied magnetic field in in-plane (IP) and out-of-plane (OP) directions, respectively. The *M-H* loops measured at 300 K are anhysteretic; coercivity starts to be noticeable at temperatures equal and lower than 250 K, indicating that T_C is located between 250 and 300 K. Figures 7(c) and 7(d) show the detail of the *M-H* loops at lower magnetic fields. One can observe that the squareness of the curves is slightly higher in the IP loops indicating that the film can be magnetized in two perpendicular directions. Rode *et al.* reported that one of the Mn sublattices, in particular that constituted by *2b* sites, has a canting towards the *a-b* plane, which produces a weak FM component in the IP *M-H* loops [17]. In our samples the simultaneous IP and OP anisotropy is due to the random orientation of the nanoparticles composing the film. The M_s in the OP loops is $M_s^\perp = 210$ kAm^{-1} and that measured in the plane is $M_s^\parallel = 180$ kAm^{-1}.
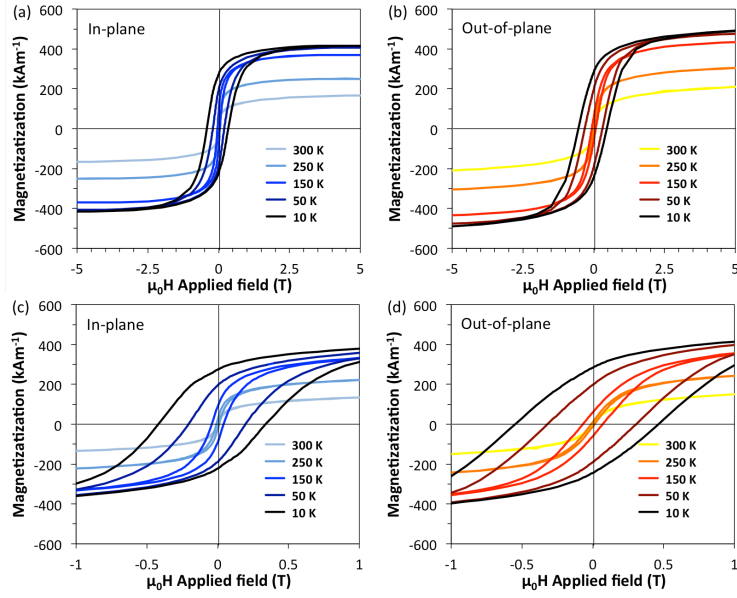
Fig. 7. SQUID *M-H* loops of the $Mn_3GaC_{0.25}$ sample at different temperatures measured in two orientations (a) in-plane and (b) out-of-plane. (c) And (d) show a detail at low fields of the loops shown in (a) and (b), respectively.

The *M-H* loops measured at different temperatures were used to accurately evaluate M_s for the IP and OP directions, as shown in Fig. 8(a). The demagnetization of FM or FiM materials at low temperatures, in particular in a range of $T < T_C/2$ is due to the excitation of the long wavelength spin waves (magnons) [18] analogous to phonons in a crystal. The energy of such spin waves is related to the stiffness constant D. The demagnetization process from $M(T = 0)$ to temperatures well below the critical temperature T_0 is characterized by the equation [19]:

$$M(T) = M(T = 0)[1 - (T/T_0)^{\alpha_B}]\tag{4}$$

where $B = (1/T_0)^{\alpha_B}$ is the Bloch's constant, $B = 2.6149 V_0 (k_B/4\pi D)^{3/2}$, V_0 being the atomic volume [19], α_B is the Bloch's exponent, and T is the absolute temperature. The fitting for FM or FiM materials obeys well to an exponent α_B equal to 3/2 for bulk samples. The data obtained from our sample is plotted in Fig. 8(a) for the IP and OP configurations.

The fitting of our sample was achieved with $\alpha_B = 2$ for both configurations. This deviation from the Bloch's law depends on the microstructure of the material [20], in particular to nanoscale effects as the long wavelength of the magnons exceed the nanometer size of the NPs composing the film and a minimum thermal energy is required to excite the spin waves. The deviation from the $\alpha_B = 3/2$ exponent in NPs is also explained by the Bose-Einstein condensation at finite temperatures. Similar deviations of the Bloch's exponent have been found in other nanoscale systems as in nickel ferrite nanoparticles [20], Fe-C amorphous particles [21] and $CuFe_2O_4$ nanoparticles [22]. In all these cases α_B is close to 2 and the deviation is also attributed to the geometric shape of the NPs and the surrounding medium (magnetizing or demagnetizing interactions between NPs) [23].

On the other hand the evolution of the dependence of the temperature on the coercive field is shown in Fig. 8(b). The fitting of the data points has been achieved using the Kneller's law [24]:

$$H_c(T) = H_c(T = 0)\left[1 - (T/T_B)^{1/2}\right] \tag{5}$$

where T_B is the blocking temperature obtained from the ZFC measurements show later in Fig. 9. The fitting for the IP and OP obtained data is achieved through a deviation of the ½ exponent along all the temperature range, the fitted values are 0.08 and 0.06, respectively. This deviation is also attributed to size effects, for example in Fe_3O_4 NPs [25]. However, other NP systems as $Mn_{0.5}Zn_{0.5}Gd_{0.02}Fe_{1.98}O_4$ show an exponent of 0.57 [26]. Nevertheless, values of the Kneller's exponents have been theoretically predicted to be between 0 and 0.5 [27]. Values near to ½ imply a non-interacting single domain NPs with uniaxial anisotropy [20]; any deviation from this value can be attributed to dipolar interactions, spin disorder at the surface of the NPs modifying the surface anisotropy of the NPs and hence the total anisotropy [28], as, for example, the IP and OP anisotropy observed on the sample. It is noteworthy that the behavior of our magnetic thin film can be fairly well described considering it formed by magnetic interacting NPs.
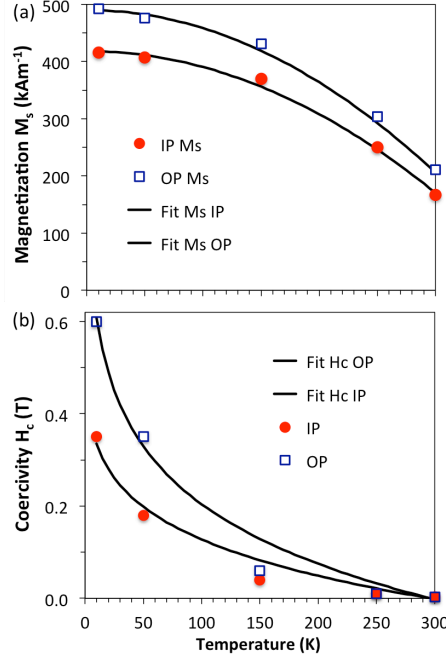
Fig. 8. Temperature dependence on (a) saturation magnetization and (b) coercivity of the Mn$_3$GaC$_{0.25}$ sample measured in the plane (IP, solid circles) and out of the plane (OP, open squares), and their corresponding fits (lines).

Figure 9 shows the ZFC-FC curves in IP and OP directions measured under an applied magnetic field of 20 mT from 5 to 380 K. Both measurements show irreversibility at around 360 K and T_B at 254 and 296 K for the IP and OP curves. The condition for superparamagnetic behavior for spherical NPs presenting uniaxial anisotropy could be expressed as $KV = 25 \, kT_B$ [29], where V is the volume of the NP, K is the anisotropy energy, and k is the Boltzmann constant. Hence, larger particles will be stable upon higher temperatures. As the volume of the crystallites is constant along both IP and OP directions, the fact that different blocking temperatures are obtained confirm the fact that the shape anisotropy and the magnetocrystalline anisotropy of the particles is not equal in both directions, and hence the dipolar interactions between crystallites are different depending the measurement direction. The increase of the value of T_B on the OP-ZFC curve is due to an increase of the bipolar interaction [30], suggesting that the film has a major tendency for an OP anisotropy, in agreement with results from Fig. 7(b).
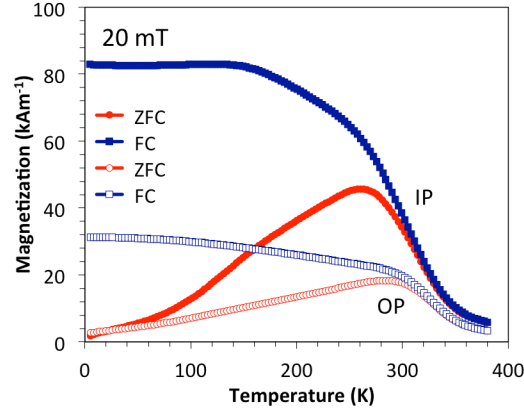
Fig. 9. Zero-field-cooled and field-cooled curves of the sample measured in IP and OP directions exhibiting different blocking temperatures.

Conclusions

We have grown polycrystalline C-doped Mn_3Ga thin films with a carbon concentration of 0.25 at.% by magnetron sputtering on $Si(001)/SiO_2$ substrates. An extensive characterization has been performed, including residual stress calculation, theoretical calculations and analysis of the saturation and coercivity of the M-H loops at different temperatures. We have found experimentally that the direction of the residual stress component is in tension, with σ_ϕ = 7880 kPa at ω = 0.5 deg. Residuals stress components of 8442 and 8443 kPa were found when the depth of x-ray beam is increased to ω = 1 and 1.5, respectively. Theoretical calculations show that spin magnetic moments of Mn atoms depend on the atomic positions and on their proximity with C atoms. The ferrimagnetic ordering is preserved on the supercell but with an additional contribution from C and Ga atoms. The main source of magnetic moments are the Mn-d orbitals. Finally, the analysis from the saturation magnetization at different temperatures shows to obey the Bloch's law, with a deviation from the 3/2 law. In particular, the Bloch exponent in our system is 2, attributed to the reduced size of the crystallites composing the film. The temperature dependence on the coercivity has been described by the Kneller's law, with fitted exponents differing from the theoretical value of 0.5. The obtained exponents for magnetic M-H loops

measured in-plane and out-of-plane directions are 0.16 and 0.04. These results indicate that dipolar interactions take place between $Mn_3GaC_{0.25}$ nanoparticles.

Acknowledgements

References

[1]   C. Yoshida, H. Noshiro, Y. Yamazaki, T. Sugii, T. Tanaka, A. Furuya, and Y. Uehara, Micromagnetic simulation of electric-field-assisted magnetization switching in perpendicular magnetic tunnel junction, AIP Advances 7 (2017) 055935.

[2]   O. Lopez Sanchez, D. Ovchinnikov, S. Misra, A. Allain, and A. Kis, Valley Polarization by Spin Injection in a Light-Emitting van der Waals Heterojunction, Nano Lett. 16 (2016) 5792.

[3]   K.S. Das, W.Y. Schoemaker, B.J. van Wees, and I.J. Vera-Marun, Spin injection and detection via the anomalous spin Hall effect of a ferromagnetic metal, Phys. Rev. B 96 (2017) 220408(R).

[4]   T.J. Nummy, S.P Bennett, T. Cardinal, and D. Heiman, Large coercivity in nanostructured rare-earth-free Mn_xGa films, Appl. Phys. Lett. 99 (2011) 252506.

[5]   R.M. Gutiérrez-Pérez, J.T. Holguín-Momaca, C.R. Santillán-Rodríguez, Ricardo López Antón, M.T. Ochoa-Lara, N.R. Flores-Holguín, F. Espinosa-Magaña, J.A. Matutes-Aquino, S.F. Olive-Méndez, High enhanced magnetization in carbon-doped Mn_3Ga thin films, Intermetallics 88 (2017) 14.

[6]   G. Kresse and J. Furthmüller, Efficient iterative schemes for ab initio total-energy calculations using a plane-wave basis set, Phys. Rev. B 54 (1996) 11169.

[7]   G. Kresse and D. Joubert, From ultrasoft pseudopotentials to the projector augmented-wave method, Phys. Rev. B 59 (1999) 1758.

[8]   P.E. Blöchl, Projector augmented-wave method, Phys. Rev. B 50 (1994) 17953.

[9]   D.D. Koelling, Linearized form of the APW method, J. Phys. Chem. Solids 33 (1972) 1335.

[10]   J.P. Perdew, K. Burke and M. Ernzerhof, Generalized Gradient Approximation Made Simple, Phys. Rev. Lett. 77 (1996) 3865.

[11]   E.T. Dias, K.R. Priolkar, A.K. Nigam, Effect of carbon content on magnetostructural properties of Mn_3GaC, J. Magn. Magn. Mater. 363 (2014) 140.

[12]   S. Wirth, A. Leither-Jasper, A.N. Vasilev, J.M.D. Coey, Structural and magnetic properties of Ni_2MnGa, J. Magn. Magn. Mater. 167 (1997) L7.

[13]   S. Ozdemir Karta, T. Cagın, Elastic properties of Ni_2MnGa from first-principles calculations, J. Alloys Compd. 508 (2010) 177.

[14] U. Welzel, J. Ligot, P. Lamparter, A.C. Vermeulen and E.J. Mittemeijer, Stress analysis of polycrystalline thin films and surface regions by X-ray diffraction, J. Appl. Cryst. 38 (2005) 1–29.

[15] A.C. Vermeulen, Assumptions in thin film residual stress methods, Mater. Sci. Forum, 404-407 (2002) 35.

[16] J. Winterlik, B. Balke, G.H. Fecher, and C. Felser, Structural, electronic, and magnetic properties of tetragonal $Mn_{3-x}Ga$: Experiments and first-principles calculations, Phys. Rev. B 77 (2008) 054406.

[17] K. Rode, N. Baadji, D. Betto, Y.-C. Lau, H. Kurt, M. Venkatesan, P. Stamenov, S. Sanvito, J. M. D. Coey, E. Fonda, E. Otero, F. Choueikani, and P. Ohresser, Site-specific order and magnetism in tetragonal Mn_3Ga thin films, Phys. Rev. B 87 (2013) 184429.

[18] A.P. Guimarães, Principles of nanomagnetism; Springer: Berlin/Heidelberg, Germany, 2009; ISBN 978-3-642-01482-6.

[19] K. Mandal, Subarna Mitra and P. Anil Kumar, Deviation from Bloch $T^{3/2}$ law in ferrite nanoparticles, Europhys. Lett., 75 (4) (2006) 618.

[20] K. Maaz, A. Mumtaz, S.K. Hasanain, M.F. Bertino, Temperature dependent coercivity and magnetization of nickel ferrite nanoparticles, J. Magn. Magn. Mater. 322 (2010) 2199–2202.

[21] S. Linderoth, L. Balcells, A. Labarta, J. Tejada, P.V. Hendriksen, S.A. Sethi, Magnetization and Mössbauer studies of ultrafine Fe-C particle, J. Magn. Magn. Mater. 124 (1993) 269–276.

[22] C.R. Alves, R. Aquino, M.H. Sousa, H.R. Rechenbrg, G.F. Goya, F.A. Tourinho, J. Depeyrot, J. Met. Nanocrys. Mater. 20–21 (2004) 694–699.

[23] S. Cojocaru , A. Naddeo and R. Citro, Modification of the Bloch law in ferromagnetic nanostructures, Europhys. Lett. 106(1) (2014) 17001.

[24]   E.F. Kneller, F.E. Luborsky, Particle Size Dependence of Coercivity and Remanence of Single‐Domain Particles, J. Appl. Phys. 34 (1963) 656.

[25] C. Nayek, K. Manna, G. Bhattacharjee, P. Murugavel and I. Obaidat, Investigating Size- and Temperature-Dependent Coercivity and Saturation Magnetization in PEG Coated Fe_3O_4 Nanoparticles, Magnetochemistry 3 (2017) 19.

[26] I.M. Obaidat, B. Issa, B.A. Albiss, and Y. Haik, Temperature Dependence of Saturation Magnetization and Coercivity in Ferrite $Mn_{0.5}Zn_{0.5}Gd_{0.02}Fe_{1.98}O_4$ Nanoparticles, Conf. Ser.: Mater. Sci. Eng. 92 (2015) 012012.

[27] J. Carrey, B. Mehdaoui, M. Respaud, Simple models for dynamic hysteresis loop calculations of magnetic single-domain nanoparticles: Application to magnetic hyperthermia optimization, J. Appl. Phys. 109 (2011) 083921.

[28] A. I. Dmitriev and A. A. Filatov, Generality of spontaneous and stimulated magnetization reversal in MnSb clusters embedded in GaMnSb thin films, physics of the solid state, 59(9) (2017) 1734–1738.

[29] B.D. Cullity and C.D. Graham, Introduction to Magnetic Materials (2nd Ed.), IEEE Press/John Wiley & Sons, 2009, p. 386.

[30] D. Kechrakos and K. N. Trohidou, Magnetic properties of dipolar interacting single-domain particles, Phys. Rev. B, 58(18) (1998) 12169.